Noname manuscript No.
(will be inserted by the editor)

Design of a Smagorinsky Spectral Vanishing Viscosity turbulence model for discontinuous Galerkin methods

Juan Manzanero · Esteban Ferrer · Gonzalo Rubio · Eusebio Valero

Received: date / Accepted: date

Abstract We present a new closure model for Large Eddy Simulation to introduce dissipation in under–resolved turbulent simulation using discontinuous Galerkin (DG) schemes applied to the compressible Navier–Stokes equations. The development of the method is based on a thorough analysis of the numerical dissipation mechanisms in DG schemes. In particular, we use upwind Riemann solvers for inter–element dissipation, and a Spectral Vanishing Viscosity (SVV) method for interior dissipation. First, these mechanisms are analysed using a linear von Neumann analysis (for a linear advection–diffusion equation) to characterise their properties in wave–number space. Second, their behaviour is tested using the three–dimensional Taylor–Green Vortex Navier–Stokes problem to assess transitional/turbulent flows. The results of the study are subsequently used to propose a DG–SVV approach that uses a mode-selection Smagorinsky LES model to compute the turbulent viscosity.

Juan Manzanero (E-mail: juan.manzanero@upm.es), Gonzalo Rubio, Esteban Ferrer, Eusebio Valero
ETSIAE-UPM - School of Aeronautics, Universidad Politécnica de Madrid. Plaza Cardenal Cisneros 3, E-28040 Madrid, Spain. // Center for Computational Simulation, Universidad Politécnica de Madrid, Campus de Montegancedo, Boadilla del Monte, 28660, Madrid, Spain.

When the SVV technique is combined with a low dissipation Riemann solver, the scheme is capable of maintaining low dissipation levels for laminar flows, while providing the correct dissipation for all wave–number ranges in turbulent regimes. The developed approach is designed for polynomial orders $N \geq 2$ and is specially well suited for high order schemes. This new DG–SVV approach is calibrated with the Taylor–Green test case; to then show its accuracy in an under–resolved ($y^+ > 8$) channel flow at Reynolds number $Re_\tau = 183$.

Keywords Discontinuous Galerkin, Energy Stable, under–resolved turbulence, Large Eddy Simulation, Smagorinsky, Spectral Vanishing Viscosity

1 Introduction

High–order discontinuous Galerkin (DG) methods have been adopted by academia and research centres as an alternative to classic numerical schemes (e.g. Finite Differences, Finite Volumes or Finite Elements). During recent years, DG methods have been adapted to solve increasingly complex physics; including incompressible, compressible, and multiphase flow problems [1, 2, 3, 4, 5, 6, 7, 8, 9]. This popularity may be attributed to two characteristics. First, DG methods provide high accuracy even for unstructured distorted meshes [10], a property difficult to retain when using classic methods (e.g. Finite Differences or Finite Volumes). This property is a result of the compactness and local character of the scheme, enabling high order accuracy with compact stencils. Second, DG methods have shown to be more robust that their high order continuous Galerkin relatives [11]. This last beneficial property has been often attributed to the use of upwind Riemann solvers, which add controlled dissipation, enhancing robustness.

In recent years, the DG community has exploited the increased robustness provided by Riemann solvers to simulate under–resolved turbulent flows, e.g. [12, 13]. This enhanced robustness rests on the localised dissipation provided by upwind Riemann solvers to dissipate small flow structures, which cannot be resolved on coarse meshes. Methods that rely on the numerics to provide mechanisms for turbulent dissipation are typically known as implicit Large Eddy Simulation (iLES) methods. The term implicit evidences that the numerical errors (in particular the dissipation) are in charge of dissipating under–resolved flow structures. An alternative to iLES is provided by explicit LES methods, where flow dissipation at small scales rests on physical arguments and modified flow equations, e.g. [14, 15]. To solve under–resolved turbulent flows using iLES/LES methods, it is necessary to understand and control numerical errors, and specially numerical dissipation introduced by the scheme, which replaces and/or complements explicit subgrid–scale models.

There are different alternatives to provide numerical dissipation in DG methods. The most popular choice is to include upwind Riemann solvers, which arise naturally from the integration by parts of the non–linear fluxes and the existence of inter–element discontinuities in DG. These fluxes introduce local dissipation, which scales with the size of the discontinuities in the numerical solution. In under–resolved flows, the size of such discontinuities increases and it has been argued (see for example [2]) that fluxes based on discontinuities may act as an appropriate stabilising mechanism for under–resolved turbulent simulations. In addition to upwind Riemann solvers, we consider the Spectral Vanishing Viscosity (SVV) technique [16] to include dissipation, when the dissipation resulting from the Riemann solver is insufficient. The SVV technique was first introduced for Fourier and continuous Galerkin discretizations [17] to regularise the solution (i.e. avoid oscillatory phenomena) in the inviscid Burg-

ers equation, and later in the Navier–Stokes Equations (NSE) [18]. The SVV provides additional dissipation complements that provided by the numerical fluxes, enhances stability, vanishes in the laminar limit and provides spectral convergence in high–order discretizations. Let us note that other techniques to introduce localised dissipation in continuous discretizations exist but are not considered in this work, e.g. SUPG stabilisation.

A substantial amount of work [2, 19, 20, 21, 22, 23, 24] has focused on understanding the stabilising effect of upwind Riemann solvers on under–resolved turbulent flows. However, limited efforts have been devoted to understanding the combined effect of Riemann solvers (i.e. interface dissipation) and discretised viscous terms (i.e. volume dissipation). In this text, we analyse the individual contribution of each term but also the combined effect. For all dissipative mechanisms, we first analyse their numerical properties in wave–number space, using von Neumann analysis on a linear advection–diffusion equation. Similar work has been presented for linear advection with constant coefficients [25, 26] and for non–constant coefficients [27]. In addition, the authors proposed, in [28], a non–modal approach as an extension to von Neumann analysis. Second, we correlate these findings with results for DNS and iLES simulations of the 3D Taylor–Green Vortex (TGV) Navier–Stokes problem with transitional/turbulent flow [12, 13].

Even though von Neumann analyses are restricted to the constant advection–diffusion equation, we will confirm, with the help of numerical experiments, that von Neumann results are consistent with observations of under–resolved Navier–Stokes turbulent flows. We show that the dissipation introduced by upwind Riemann solvers affects high wave–numbers (around 75% of the Nyquist wave–number), while discrete second order derivatives provide dissipation at low and medium wave–numbers (around 25% and 50% of the Nyquist wave–

number respectively). Additionally, the dissipation introduced by the SVV operator helps to control the amount of dissipation introduced in the low and medium wave–number range, and provides a suitable mechanism to develop new models, as the one proposed in the final section of this manuscript.

To perform these studies, we start from a baseline scheme without dissipation (i.e. an energy conserving scheme), and include numerical dissipation through the different stabilisation techniques. In the linear advection equation with constant coefficient it suffices to consider central fluxes (see [29, 30]), but in the non–linear Navier–Stokes equations, it is required to use split formulations [31, 32, 33], which provide kinetic energy consistency and enhances robustness.

Having quantified numerical errors for the above dissipative mechanisms, in a final section, we combine upwind Riemann solvers and SVV. Following the suggestion of Karamanos and Karniadakis for continuous Galerkin methods [18, 34], we modify the classic SVV technique using a Smagorinsky model to adjust the amount of dissipation introduced. This new proposed DG model is capable of maintaining low dissipation levels in laminar flows, while modelling small eddies and providing correct dissipation for all wave–number ranges in turbulent regimes.

The rest of this paper is organised as follows: we describe the dissipative mechanisms and their inclusion in the one–dimensional advection–diffusion and three–dimensional Navier–Stokes equations in Section 2. In Section 3, we study two dissipation techniques: Section 3.2 analyses interface dissipation (upwind Riemann solvers) while Section 3.3 investigates internal dissipation (discrete second order derivatives and SVV). Finally, we propose and test a Smagorinsky–SVV DG discretization to simulate under–resolved turbulent/transitional flows in Section 4.

2 Methodology

We first present, in Section 2.1, the one–dimensional advection–diffusion equation for the discrete DG approximation and the von Neumann stability analysis. In Section 2.2 we present the DG discretization of the three–dimensional compressible Navier–Stokes equations. Then, in Section 2.3, we briefly introduce energy conserving schemes. Finally, in Section 2.4, we detail how the dissipation mechanisms are included both in the Navier–Stokes equations and in the advection–diffusion equation.

2.1 One–dimensional advection–diffusion equation and von Neumann Analysis

The one–dimensional linear advection–diffusion equation is

$$u_t + a u_x = (\mu u_x)_x, \quad 0 \leqslant x \leqslant 1, \tag{1}$$

where a is a constant advection speed and μ is the viscosity.

To perform von Neumann analysis we introduce an exponential wave solution, with spatial wave–number k and temporal frequency ω,

$$u(x,t) = e^{ikx - i\omega t} = u_0(x) e^{-i\omega t}, \tag{2}$$

with $u_0(x) = e^{ikx}$ the part of (2) that only depends on the spatial coordinate. The relationship between the temporal frequency and the spatial wavenumber, $\omega(k)$, is such that yields an eigenfunction of the original partial differential equation (1). To obtain the relationship $\omega(k)$ we introduce (2) in (1),

$$-i\omega e^{ikx - i\omega t} + iake^{ikx - i\omega t} = -\mu k^2 e^{ikx - i\omega t}, \quad \omega(k) = ak - i\mu k^2. \tag{3}$$

The original equation (1) advects the initial condition (2) keeping a constant speed a, and decreases its amplitude at a rate given by μk^2. Von Neumann analysis consists in the use of the same initial condition (2) in the discrete version of (1) to obtain the numerical relation $\omega(k)$. On the contrary to the continuous equation, the discrete operator will incur errors on the propagation speed and errors on the amplitude of the wave, which will not be kept constant. The change of the wave amplitude of the discrete solution is related with the stability of the numerical scheme. A scheme whose solutions' amplitude grows infinitely ($\mathrm{Im}\,(w) > 0$) is said to be unstable, while a dissipative scheme obtains $\mathrm{Im}\,(w) \leqslant -\mu k^2$. Because of the linear relation between spatial and temporal frequencies, without loss of generality we will only study a constant coefficient $a = 1$.

We consider the DG discretization of the linear advection equation (1) in an uniform grid that divides the physical domain $[0, 1]$ in elements with spacing h. Here we briefly highlight the steps that construct a DG formulation, and the interested reader can find more details in [35]. In each element e, we approximate the solution with an order N polynomial,

$$u\,(x,t)_e \approx \mathrm{I}^N\left(u\big|_e\right) = U^e\,(\xi,t) = \sum_{j=0}^{N} U_j(t) l_j\,(\xi)\,, \tag{4}$$

written using the Lagrange polynomials $l_j\,(\xi)$ in a set of interpolation nodes $\{\xi_i\}$ that range in a local reference element $\xi \in [-1, 1]$. Next, we construct a weak form of the advection equation (1) on the element e. To do so, we first write the second order equation as a system of two first order equations with the definition of the auxiliary variable $g = u_x$. Next, we refer the derivative operators to the reference space $u_\xi = \frac{h}{2} u_x$. Then we multiply (1) and $\frac{h}{2} g = u_\xi$ by an arbitrary N order polynomial ϕ and integrate them in the reference

element $[-1,1]$ to obtain,

$$\begin{aligned}
&\frac{h}{2}\int_{-1}^{1} u_t\phi\,\mathrm{d}\xi + au\phi\big|_{-1}^{1} - \int_{-1}^{1} au\phi_\xi\,\mathrm{d}\xi = \mu g\phi\big|_{-1}^{+1} - \int_{-1}^{1}\mu g\phi_\xi\,\mathrm{d}\xi,\\
&\frac{h}{2}\int_{-1}^{1} g\phi\,\mathrm{d}\xi = u\phi\big|_{-1}^{1} - \int_{-1}^{1} u\phi_\xi\,\mathrm{d}\xi,
\end{aligned} \tag{5}$$

where the two terms that contain spatial derivatives have been integrated by parts. Now, we replace the continuous functions by their polynomial approximations, and we replace the exact integrals by a Gaussian quadrature rule based on the same interpolation nodes $\{\xi_i\}$, with weights $\{w_i\}$,

$$\begin{aligned}
&\frac{h}{2}\int_{-1,N}^{1} U_t\phi\,\mathrm{d}\xi + (aU)^\star\phi\big|_{-1}^{1} - \int_{-1,N}^{1} aU\phi_\xi\,\mathrm{d}\xi = \mu G^\star\phi\big|_{-1}^{+1} - \int_{-1,N}^{1}\mu G\phi_\xi\,\mathrm{d}\xi,\\
&\frac{h}{2}\int_{-1,N}^{1} G\phi\,\mathrm{d}\xi = U^\star\phi\big|_{-1,N}^{1} - \int_{-1}^{1} U\phi_\xi\,\mathrm{d}\xi.
\end{aligned} \tag{6}$$

As a result of the discrete ansatz, the solutions are discontinuous at the inter–element boundaries. Thus, we replace the interface solution by an unique value $U^\star$, $G^\star$, taking into account the solution from both sides. The numerical flux couples the solution in adjacent elements. We define $\mathbf{U}^e = (U_0^e, U_1^e, ..., U_N^e)$ as the vector that contains the $N+1$ nodal values of the polynomial approximation of the solution in the element e. As a result, the DG scheme (6) can be summarized as,

$$\begin{aligned}
&\mathbf{U}_t^e = [\mathbf{L}_a]\mathbf{U}^{e-1} + [\mathbf{C}_a]\mathbf{U}^e + [\mathbf{R}_a]\mathbf{U}^{e+1} + [\mathbf{L}_g]\mathbf{G}^{e-1} + [\mathbf{C}_g]\mathbf{G}^e + [\mathbf{R}_g]\mathbf{G}^{e+1},\\
&\mathbf{G}^e = [\mathbf{L}_u]\mathbf{U}^{e-1} + [\mathbf{C}_u]\mathbf{U}^e + [\mathbf{R}_u]\mathbf{U}^{e+1},
\end{aligned} \tag{7}$$

where, in the linear advection–diffusion equation all the matrices are constant in time. We can replace $\mathbf{G}^e$ from the second equation to the first to obtain a

single equation,

$$\mathbf{U}_t^e = [\mathbf{LL}]\mathbf{U}^{e-2} + [\mathbf{L}]\mathbf{U}^{e-1} + [\mathbf{C}]\mathbf{U}^e + [\mathbf{R}]\mathbf{U}^{e+1} + [\mathbf{RR}]\mathbf{U}^{e+2}. \tag{8}$$

Common choices for the numerical fluxes are central and upwind fluxes for advective terms, and the Bassi–Rebay 1 or the Interior Penalty (IP) method for diffusive terms, summarized in Table 1. Insights on the properties that can be derived from the different options can be found in [36].

Table 1 Numerical fluxes used in this work for advective and diffusive terms

Advective $(aU)^\star$		Diffusive $U^\star$		Diffusive $G^\star$	
Central $\lambda = 0$	Upwind $\lambda = 1$	BR1	IP	BR1	IP
$\{\!\{U\}\!\} + \frac{1}{2}\lvert a\rvert\lambda\,(U_L - U_R)$		$\{\!\{U\}\!\}$	$\{\!\{U\}\!\}$	$\{\!\{G\}\!\}$	$\{\!\{\nabla U\}\!\} - \sigma\,(U_L - U_R)$

We describe von Neumann analysis applied to the DG scheme (8), which is also valid for any scheme written in matricial form. Further details on the derivation of von Neumann analysis for an advection–diffusion equation can be found in [37, 27]. The choice of the initial condition, and the linearity of the equation, allows us to relate the solution in neighboring elements to one reference element,

$$\mathbf{U}^{e-n} = e^{-iknh}\mathbf{U}^e. \tag{9}$$

We introduce (9) in the discrete equation (8) to obtain a linear ordinary differential equation system for each individual element,

$$\frac{h}{2}\frac{d\mathbf{U}^e}{dt} = \left(e^{-2ikh}[\boldsymbol{LL}] + e^{-ikh}[\boldsymbol{L}] + [\boldsymbol{C}] + e^{ikh}[\boldsymbol{R}] + e^{2ikh}[\boldsymbol{RR}]\right)\mathbf{U}^e = [\boldsymbol{M}(kh)]\mathbf{U}^e. \tag{10}$$

The general solution of (10) is linearly spanned by the $N+1$ modes of the eigenvalue problem (note that, for simplicity, the index e has been dropped),

$$-i\omega_m \frac{h}{2}\mathbf{V}_m = [\boldsymbol{M}(kh)]\mathbf{V}_m, \quad \mathbf{U}(t) = \sum_{m=0}^{N} A_m \mathbf{V}_m e^{-i\omega_m t}, \tag{11}$$

where $\mathbf{V}_m$ are the unitary eigenvectors, and the amplitudes A_m are constants computed to recover the initial condition in $t=0$,

$$\mathbf{U}(0) = \mathbf{U}_0 = e^{ik\mathbf{x}} = \sum_{m=0}^{N} A_m \mathbf{V}_m. \tag{12}$$

The solution structure (12) allows us to classify three different numerical error sources, which were already detailed in [26, 27]. Specifically, only the so-called *primary mode* (p) propagates with the physical wave-speed and damping (e.g. $\omega_p = 0$ when $k=0$). Hence, we rewrite the solution isolating the primary mode contribution from the remaining modes (called *secondary modes*, $m \neq p$),

$$\mathbf{U} = A_p \mathbf{V}_p e^{-i\omega_p t} + \sum_{\substack{m=0 \\ m\neq p}}^{N} A_m \mathbf{V}_m e^{-i\omega_m t}. \tag{13}$$

Next, the initial condition (12) is also separated in the contribution of primary and secondary modes, and introduced in (13). As a result, we can consider the numerical solution as the primary mode propagating the initial condition, $\mathbf{U}_0 e^{-i\omega_p t}$, and the non–physical errors (which propagate with both primary and secondary mode speeds) as secondary modes, $\Delta\mathbf{U}(t)$,

$$\begin{aligned}\mathbf{U} &= \mathbf{U}_0 e^{-i\omega_p t} + \sum_{\substack{m=0 \\ m\neq p}}^{N} A_m \mathbf{V}_m \left(e^{-i\omega_m t} - e^{-i\omega_p t}\right) \\ &= \mathbf{U}_0 e^{-i\omega_p t} + \Delta\mathbf{U}(t).\end{aligned} \tag{14}$$

The numerical propagation speed experienced by the initial condition, $\mathbf{U}_0$, (i.e. the primary mode frequency, ω_p) will differ from that dictated by the analytical PDE ($\omega = ak$). The difference between its real part and the theoretical travelling speed, ak, will yield a dispersion error (i.e. error in the propagation speed), while its imaginary part, which is generally non–zero, entails numerical dissipation. Following [26], we define the non–dimensional wave–number, $\hat{k}$, as

$$\hat{k} = \frac{kh}{N+1}, \tag{15}$$

such that we will distinguish between low wave–numbers ($\hat{k} \lesssim \pi/4$), medium wave–numbers ($\hat{k} \sim \pi/2$) and high wave–numbers ($\hat{k} \gtrsim 3\pi/4$), with respect to Nyquist wave–number ($\hat{k} = \pi$). Further details on the discretization and analysis of the one–dimensional advection equation and extended von Neumann analysis for advection equations with non–constant coefficients may be found in other works by the authors in [27, 30, 38].

2.2 Three–dimensional compressible Navier–Stokes equations

We write the three–dimensional compressible Navier–Stokes equations in compact form,

$$\mathbf{u}_t + \nabla \cdot \boldsymbol{F}_e(\mathbf{u}) = \nabla \cdot \boldsymbol{F}_v(\mathbf{u}, \nabla\mathbf{u}), \tag{16}$$

where $\mathbf{u}$ is the vector of conservative variables $\mathbf{u} = [\rho, \rho v_1, \rho v_2, \rho v_3, \rho e]^T$. Details on the specific formulations retained for inviscid $\boldsymbol{F}_e$ and viscous $\boldsymbol{F}_v$ fluxes can be found in Appendix A of this text.

To derive discontinuous Galerkin schemes, we consider (16) for one mesh element e, we multiply it by an arbitrary order N polynomial ϕ, and integrate on e,

$$\int_e \mathbf{u}_t \phi + \int_e \nabla \cdot \boldsymbol{F}_e \phi = \int_e \nabla \cdot \boldsymbol{F}_v \phi. \tag{17}$$

We integrate by parts the fluxes integrals to obtain a local weak form of the equations (one per mesh element), and approximate the integrals by Gauss quadratures,

$$\int_{e,N} \mathbf{u}_t \phi + \int_{\partial e,N} \boldsymbol{F}_e \cdot \mathbf{n} \phi - \int_{e,N} \boldsymbol{F}_e \cdot \nabla \phi = \int_{\partial e,N} \boldsymbol{F}_v \cdot \mathbf{n} \phi - \int_{e,N} \boldsymbol{F}_v \cdot \nabla \phi, \tag{18}$$

where $\mathbf{n}$ is the normal vector at element boundaries ∂e. We replace discontinuous fluxes at inter–element faces by a numerical inviscid flux, $\mathbf{F}_i^\star$, to obtain a weak form for the equations for each element,

$$\int_{e,N} \mathbf{u}_t \phi + \int_{\partial e,N} \mathbf{F}_e^\star \cdot \mathbf{n} \phi - \int_{e,N} \boldsymbol{F}_e \cdot \nabla \phi = \int_{\partial e,N} \mathbf{F}_v^\star \cdot \mathbf{n} \phi - \int_{e,N} \boldsymbol{F}_v \cdot \nabla \phi, \tag{19}$$

Since we are using split–form schemes, we follow [31] to get a weak–strong form using the summation–by–parts property on the inviscid fluxes in (19),

$$\int_{e,N} \mathbf{u}_t \phi + \int_{\partial e,N} (\mathbf{F}_e^\star - \mathbf{F}_e) \cdot \mathbf{n} \phi + \int_{e,N} \nabla \cdot \boldsymbol{F}_e \phi = \int_{\partial e,N} \mathbf{F}_v^\star \cdot \mathbf{n} \phi - \int_{e,N} \boldsymbol{F}_v \cdot \nabla \phi, \tag{20}$$

where the divergence of inviscid fluxes $\nabla \cdot \mathbf{F}_e \approx \mathbb{D} \left(\mathbf{F}_e\right)^{\mathrm{PI}}$ is computed using Pirozzoli's two–point kinetic energy preserving flux (see [31] and Appendix A for details). Finally, we augment viscous fluxes with the spectral vanishing

Table 2 Summary of dissipative mechanisms: $\hat{k}$ denotes the non–dimensional wave–number, $\hat{k} = kh/(N+1)$.

Mechanism	Discretization	Section	Dissipation range
Interface dissipation	upwind, Roe, low dissipation Roe [39]	2.4.1 3.2	High wave–numbers ($\hat{k} > \pi/2$)
Volume dissipation	LES models, SVV	2.4.2 3.3	Low ($\hat{k} < \pi/2$) to medium ($\hat{k} \sim \pi/2$) wave–numbers and tuneable for SVV

viscosity $\mathbf{F}_{v+} = \mathbf{F}_v + \mathbf{F}_{\mathrm{SVV}}$,

$$\int_{e,N} \mathbf{u}_t \phi + \int_{\partial e,N} \left(\mathbf{F}_e^\star - \mathbf{F}_e\right) \cdot \mathbf{n}\phi + \int_{e,N} \mathbb{D}\left(\mathbf{F}_e\right)^{\mathrm{PI}} \phi = \int_{\partial e,N} \mathbf{F}_{v+}^\star \cdot \mathbf{n}\phi - \int_{e,N} \boldsymbol{F}_{v+} \cdot \nabla\phi, \tag{21}$$

Details on the precise forms of such terms are included in following sections. Additionally, Table 2 summarises the various dissipative mechanisms and details their effect in the wave–numbers space.

Further details regarding the nodal discontinuous Galerkin formulation used in this paper may be found in [35, 31, 32] for three–dimensional unstructured grids with curved elements.

2.3 Briefly on energy preserving schemes

Throughout the paper we use only kinetic energy preserving schemes, where the kinetic energy can not increase as a result of the physical and numerical dissipation [40]. Because the schemes are designed to remain stable and to be energy preserving, they do not require extra numerical dissipation for robustness. Hence, including numerical dissipation to these schemes enables the analysis of dissipation techniques, whose effect will not be masked by other numerical errors inherent to non–linear terms discretization. Overall, these schemes are useful to understand numerical dissipation requirements, and thus, to design robust dissipation techniques capable to achieve accurate

solutions. The dissipation techniques studied herein are the use of upwind Riemann solvers and the addition of a turbulent viscosity (e.g. LES models and spectral vanishing viscosity).

Because in the linear advection equation the volume quadratures are exactly computed, energy conserving schemes are achieved with an appropriate choice of the numerical flux. Namely, the numerical flux (see Table 1) is designed such that the first part (central fluxes) balances volume terms to obtain an energy conserving scheme (for constant advection speeds). Hence, we will refer to the particular case with $\lambda = 0$ as central fluxes (see Table 1).

The extension to the non–constant advection speed and non–linear problems (e.g. the Navier–Stokes equations) needs special treatment of volume integrals (to use split–forms) and requires the use of Gauss–Lobatto points to cancel out boundary terms using the Summation–By–Parts Simultaneous–Approximation–Term properties (SBP–SAT). The interested reader is referred to [41, 29, 27, 31] for particular split–forms for non–constant advection, Burgers and Euler equations.

2.4 Description of the dissipation mechanisms

In this section, we introduce two dissipation mechanisms found in DG methods: the interface dissipation through the numerical flux in Section 2.4.1 and the internal dissipation through the use of a turbulent viscosity methods in Section 2.4.2. We correlate the effect of these mechanisms in the one–dimensional advection–diffusion equation, to their counterparts in the three–dimensional Navier–Stokes equations, such that in following sections, the information extracted from von Neumann analyses can be used to understand the behaviour when solving laminar/turbulent flows.

2.4.1 Interface dissipation through the numerical flux

Discontinuous Galerkin methods add dissipation through the numerical flux, $\mathbf{F}_e^\star$, (see (21)), that acts in the interfaces. For the one–dimensional linear advection equation with constant coefficient (1), we use the general λ flux defined in Table 1. As demonstrated in [29], the numerical dissipation introduced by an upwind Riemann solver is proportional to the square of the solution inter–element jumps $[\![u]\!] = u_R - u_L$,

$$\left(\frac{1}{2}U^2\right)_t = -\lambda\frac{1}{2}|a|[\![u]\!]^2 \leqslant 0. \tag{22}$$

Additionally, note that λdiss vanishes when considering the analytical (smooth) solution (zero jumps), thus not altering the underlying physics in well resolved cases. We will investigate the effect of this non–linear dissipation through von Neumann analyses. These non–linearities arise as a result of the penalisation on the size of the interface jumps when increasing λ.

In the three–dimensional Navier–Stokes equations (16), inviscid fluxes or Riemann solvers are usually constructed as the average of both adjacent states, plus an interface dissipation that depends on the two states $(\mathbf{U}_L, \mathbf{U}_R)$ [42],

$$\boldsymbol{F}_e^\star \cdot \boldsymbol{n} = \{\!\{\boldsymbol{F} \cdot \boldsymbol{n}\}\!\} - \mathrm{diss}(\mathbf{U}_L, \mathbf{U}_R). \tag{23}$$

In this paper, we will consider Roe dissipation,

$$\mathrm{diss}_{Roe}(\mathbf{U}_L, \mathbf{U}_R) = \sum_{e=1}^{5} \alpha_e|\beta_e|\mathbf{K}_e, \tag{24}$$

where the intensities α_e, eigenvalues β_e and eigenvectors $\mathbf{K}_e$ are computed from the Roe averaged states [42]. We will study the effect of the parameter λ in (22) in the Navier–Stokes equations by modifying (23) to,

$$\boldsymbol{F}^{\star}\cdot\boldsymbol{n} = \{\!\{\boldsymbol{F}\cdot\boldsymbol{n}\}\!\} - \lambda \mathrm{diss}(\mathbf{U}_L, \mathbf{U}_R), \tag{25}$$

to control the dissipation added through cell interfaces with the free parameter λ. This new expression (25) compares to the linear advection form (see Table 1). Moreover, this strategy has been already adopted to design low dissipation versions for Roe Riemann solvers which provide an appropriate estimate for λ [39]. Nonetheless in the $\mathrm{L}^2\mathrm{R}$ Riemann solver derived in [39] there is a subtle difference, since this atenuation is only applied to the velocities, and not to the pressure, since the pressure atenuatation leads to pressure oscillations (see [20]).

2.4.2 Internal dissipation with spectral vanishing viscosity

We complement the dissipation provided by the interface numerical flux with additional dissipation in the interior of the elements. A framework is presented here to study the Spectral Vanishing Viscosity (SVV) method.

This technique was initially introduced to stabilise Fourier spectral methods in [17], and later adapted to high–order continuous Galerkin methods in [18]. This technique considers a constant viscosity, μ_{SVV}, which is applied unevenly on the different modes that form the solution. The operator that chooses the intensity of each mode in the dissipation is called the viscous kernel Q_μ. Precisely, we add F_{SVV} to the the one–dimensional linear advection equation to introduce the SVV regularisation,

$$F_{\mathrm{SVV}} = \mu_{SVV} Q_\mu \star \frac{\partial u}{\partial x}, \tag{26}$$

where the operator $\star$ denotes the modal convolution operator, applied to the solution derivative and the SVV viscous kernel (see implementation details in

[18]). The resulting approach can be identified as a high–pass filtered dissipation. The spectral distribution of the viscosity is defined *ad-hoc* in the viscous kernel, Q_μ, of the SVV method. In this work we adopt the kernel introduced recently by Moura et al. [37], who considered a power law,

$$Q_\mu(k) = (k/N)^{P_{SVV}}, \quad k = 0, 1, \ldots, N. \tag{27}$$

In (27), the constant P_{SVV} is the kernel power coefficient, and k is the polynomial mode index. This kernel is convenient since a standard viscous discretization is recovered when $P_{SVV} = 0$ (see (26) and (27)) and the dissipation is restricted to the highest order mode if $P_{SVV} >> 1$. Therefore, with the framework we can study both the SVV and a standard second order derivative, which serves as a point of reference. A graphical representation of the kernel (27) can be found in Figure 1.

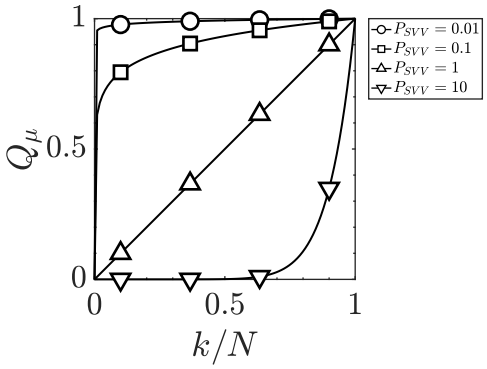

Fig. 1 Representation of the power law kernel (27) for several P_{SVV} values. The higher the kernel power coefficient P_{SVV}, the higher is the filtering performed in the viscous tensor

The SVV has been widely adopted and studied for continuous Galerkin and Fourier spectral methods [43, 16, 37, 2]. In [37], Moura et al. performed the dispersion–dissipation analysis of the continuous Galerkin SVV, finding similarities between the numerical dissipation introduced to that obtained using

upwind Riemann solvers in discontinuous Galerkin methods. However, for discontinuous Galerkin methods there are not SVV studies available. One reason would be that the SVV was introduced to achieve similar dissipation behaviour in continuous Galerkin (where the schemes present lack of numerical dissipation) to that obtained with upwind Riemann solvers in DG. Therefore, it may be naively argued that it is pointless to introduce an SVV method in DG, since the upwind fluxes achieve similar results, resulting in a more efficient and simpler implementation. However, in this paper we show that the SVV method is useful not as a substitute of upwind Riemann solvers, but as a complement of the latter to adjust energy accumulations in medium wave–numbers, which can not be controlled by the numerical flux.

In the compressible Navier–Stokes equations (see Appendix A), the SVV method is implemented by defining the following dissipation operator in (21),

$$\boldsymbol{F}_{\mathrm{SVV}} = \begin{bmatrix} 0 & 0 & 0 \\ \hat{\tau}_{xx} & \hat{\tau}_{xy} & \hat{\tau}_{xz} \\ \hat{\tau}_{yx} & \hat{\tau}_{yy} & \hat{\tau}_{yz} \\ \hat{\tau}_{zx} & \hat{\tau}_{zy} & \hat{\tau}_{zz} \\ \sum_{j=1}^{3} v_j \hat{\tau}_{1j} + k\hat{T}_x & \sum_{j=1}^{3} v_j \hat{\tau}_{2j} + k\hat{T}_y & \sum_{j=1}^{3} v_j \hat{\tau}_{3j} + k\hat{T}_z \end{bmatrix}, \tag{28}$$

where hatted variables represent those with the SVV operator applied, e.g., for viscous stresses,

$$\hat{\tau}_{ij} = \mu_{SVV} Q_\mu \star \left[\partial_j v_i + \partial_i v_j - \frac{1}{3} \delta_{ij} \partial_i v_i \right]. \tag{29}$$

We also give in this section a brief introduction to LES models. LES models introduce a solution dependent viscosity, μ_t, usually through a second order derivative. The standard Smagorinsky subgrid–scale model for the Navier–

Stokes equations [44], is used in all studies shown in this paper. Namely, $\boldsymbol{F}_{LES}$ in (21) is,

$$\boldsymbol{F}_{LES} = \boldsymbol{F}_v(\mu = \mu_t, \mathbf{v}, \nabla\mathbf{v}), \tag{30}$$

where $F_v(\mu, \mathbf{v}, \nabla\mathbf{v})$ is the Navier–Stokes viscous flux defined in (37). The Smagorinsky viscosity is defined as,

$$\mu_t = C_S^2 \Delta^2 |\boldsymbol{S}|. \tag{31}$$

The classical value for isotropic turbulence, $C_S = 0.2$, is selected while the filter width Δ is computed as in [20],

$$\Delta^3 = \frac{\text{Cell volume}}{(N+1)^3}, \tag{32}$$

which accounts for both the mesh elements size and the polynomial order. The effect of the Smagorinsky model will be analysed in detail in Section 4.

We first study the dissipation introduced by the SVV operator with a constant viscosity μ_{SVV}, and then, we construct a Smagorinsky–SVV LES scheme that uses the Smagorinsky model as the SVV viscosity $\mu_{SVV} = \mu_S$.

3 Numerical Results

We now study the two dissipation mechanisms (interface and internal) introduced in the previous section by two means: performing a linear von Neumann analysis, and solving the Taylor–Green vortex problem. Von Neumann analysis gives a global vision of the behaviour of the linear advection–diffusion equation scheme in the wave–number domain independently of the initial condition. In contrast, the TGV problem, see Appendix B, allows us to study the

dissipation introduced numerically by inspecting the kinetic energy spectra of the flow. This section is organised with the same structure as Section 2.4; we first study energy conserving schemes to establish the baseline state, to then analyse the two dissipation techniques introduced in Sections 2.4.1 and 2.4.2.

3.1 Preliminaries on kinetic energy preserving schemes

We start by considering a kinetic energy preserving scheme. We study the constant speed advection equation with Gauss points and central fluxes (diffusion is not considered here). The choice of Gauss points for this von Neumann analysis is adopted since it represents a more traditional and widely used approach, but we found that all the conclusions hold with Gauss–Lobatto points (see [25] for details).

3.1.1 Von Neumann analysis

Numerical dispersion and dissipation errors are depicted in Figures 2(a) and 2(b) respectively. We have highlighted the mode that satisfies $\mathrm{Re}\,(\omega) = 0$ for $\hat{k} = 0$ with a black line. The dashed line in Figure 2(a) depicts the analytical PDE speed (i.e. the straight line $Re(\omega) = k$). There are three groups of modes: first, grey modes in Figure 2(a) are an exact traslation of the black mode, therefore, they do not predict accurately the advection speed, and consequently they introduce numerical errors in the solution. Second, brown modes are medium-frequency modes that incur numerical errors in the propagation speed, except a narrow region close to $kh/(N+1) \simeq \pm\pi/2$, where these modes follow the analytical propagation speed. Third, blue lines represent non–physical high frequency modes. These results are in agreement with those previously reported in [10].

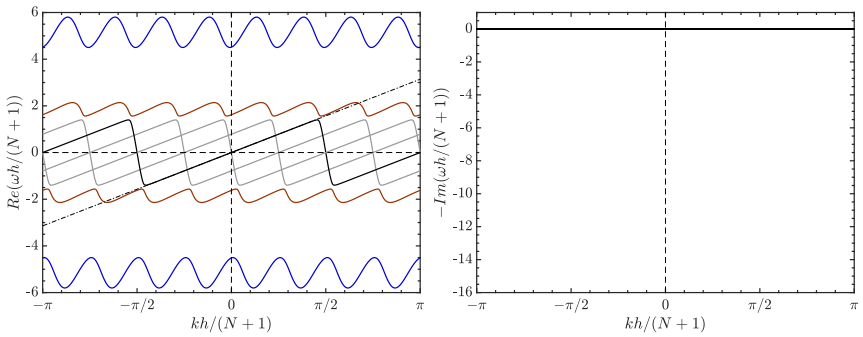

(a) Dispersion error (b) Diffusion error

Fig. 2 Dispersion-dissipation errors in the advection equation. Figures depict the eigenvalues obtained with an energy conserving DG (i.e. with central fluxes, $\lambda = 0$) and polynomial order $N = 7$

Figure 2(b) shows the dissipation errors, where neither numerical energy decay nor growth are experienced (i.e. the scheme is energy conserving, $Im(\omega) = 0$). This result is consistent with numerical energy estimates: the scheme is energy conserving since the discrete energy balance inside the computational domain vanishes (when considering constant advection speeds, [29, 30]).

3.1.2 Navier–Stokes TGV problem

We run the inviscid Taylor–Green vortex (with Mach number $M_0 = 0.1$, see Appendix B) with the kinetic energy preserving scheme (detailed in Appendix A). We consider a coarse Cartesian 8^3 mesh and fourth order ($N = 4$) polynomials.

Figure 3 depicts the kinetic energy spectra after 14 time units. We find an undesired accumulation of energy in high wave–numbers as a result of the undissipated kinetic energy transferred from large to small eddies (i.e. the scheme is energy preserving). The solution is severely under–resolved, where high wave–number modes energy (with large dispersion errors) are not dissipated. Note that this is be inferred from von Neumann analyses (see Figure 2).

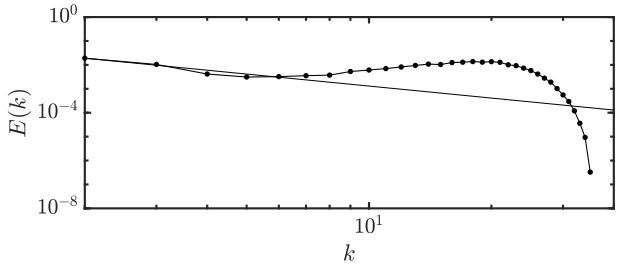

Fig. 3 Kinetic energy spectra of the inviscid Taylor–Green vortex problem (with Mach number $M_0 = 0.1$) in $t = 14$, alongside the theoretical Kolmogorov's solution $k^{-5/3}$ [45]. This result has been obtained with the energy conserving DG scheme introduced in [31]. We find that the lack of dissipation leads to energy accumulation in high wave–numbers, where the solution is severely under–resolved

A solution that presents large number of high wave–number spectral components, sees an accumulation of energy since, at these wave–numbers, dispersion errors are important in a region where there is no dissipation that drains the energy. Moreover, as a result of the insufficient energy drain, this accumulation is also transferred to lower wave–numbers by the non–linear terms of the Navier–Stokes equations. Following sections study several techniques to introduce numerical dissipation in appropriate scales, and correct this behaviour. Note that the scheme is stable without numerical dissipation, that is only added in this work to enhance the accuracy of the method.

3.2 Interface dissipation through the numerical flux

In this section, we study the effect on the scheme stability and accuracy of upwind Riemann solvers, by varying λ on $(aU)^\star$ in Table 1 for the linear advection equation and in (24) for the compressible Navier–Stokes equations. We consider the inviscid version of both the linear advection ($\mu = 0$), and the compressible Navier–Stokes (Euler equations) $\mathbf{F}_{v+} = 0$.

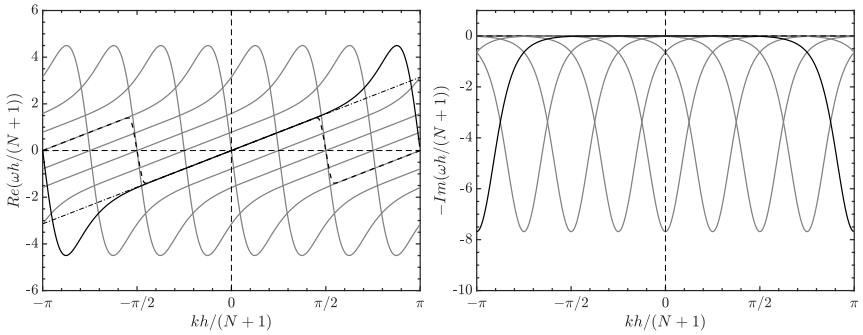

(a) Dispersion error (b) Dissipation error

Fig. 4 Dispersion and dissipation errors with $\lambda = 1.0$

3.2.1 Von Neumann analysis

We now study the dispersion and dissipation errors obtained for the upwind Riemann solver. In the previous section, we studied the central Riemann solver, that obtains a dissipation–free scheme. With an upwind Riemann solver, we start introducing numerical dissipation to the scheme.

The dispersion and dissipation errors for the upwind Riemann solver are represented in Fig. 4. This result can also be found in other works [10, 37, 25, 23], and shows the typical DG numerical dissipation: the dissipation concentrates in high wave–numbers, and it vanishes in the small wave–numbers, with a very flat region near $\hat{k} = 0$. Moreover, with the upwind Riemann solver all modes describe the same behavior (with a phase shift), which might be regarded as optimal from the point of view of time–stepping limitations in explicit or implicit–iterative solvers.

We now discuss the effect of $\lambda \neq 1$. We reckon $\lambda = 1$ as upwind fluxes, but other λ values are possible. From (22) it can be wrongly inferred that the dissipation is proportional to λ, and that we can increase and tune the numerical dissipation to the desired levels by modifying λ appropriately. This is

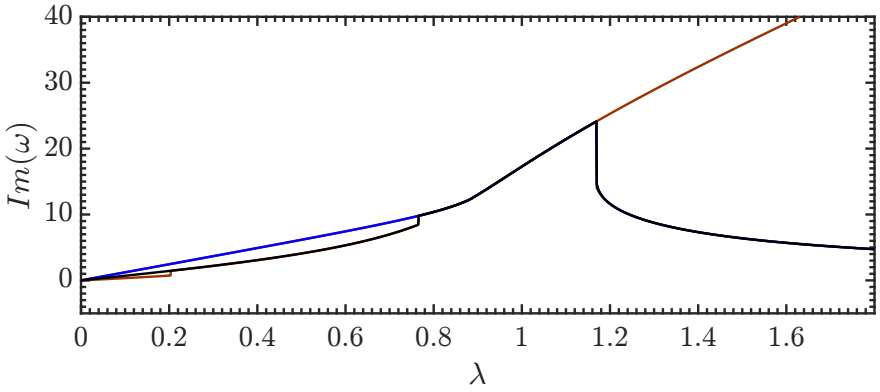

Fig. 5 Diffusion of the different mode sets, and the effect of the Riemann solver parameter λ. This representation allows us to follow the different bifurcation points that change the behaviour of the scheme dissipation. The colours represent the different mode groups identified in Figure 2(a). The precise values for the cases studied in the TGV (next section) are 0.7038 ($\lambda = 0.1$), 17.27 ($\lambda = 1$), 0.4065 ($\lambda = 10$)

not the case, however, since the dissipation obtained varies non–linearly with λ, because the inter–element jumps decrease as λ increases. The maximum dissipation experienced by the different modes as λ increases is represented in Fig. 5. We see that for lower λ values, the dissipation increases approximately linearly. We have represented the dissipation introduced by all the modes, and the mode that recovers $\omega = 0$ for $\hat{k} = 0$ is colored in black. Next, in the range $\lambda \approx 1$, all the modes are replications of the physical (primary) mode, and we obtain a configuration similar to Fig. 4(b) where the peak of dissipation increases with λ. Finally, for $\lambda > 1.2$ the dissipation of all the modes (including the mode that recovers $\omega = 0$ for $\hat{k} = 0$) decreases with λ. Thus, it is convenient to use a λ value below $\lambda \lesssim 1$, so that the numerical flux truly introduces numerical dissipation to the scheme.

3.2.2 Navier–Stokes TGV problem

In the linear von Neumann analysis we have found that upwind Riemann solvers concentrate their dissipation in high wave–numbers. This behaviour

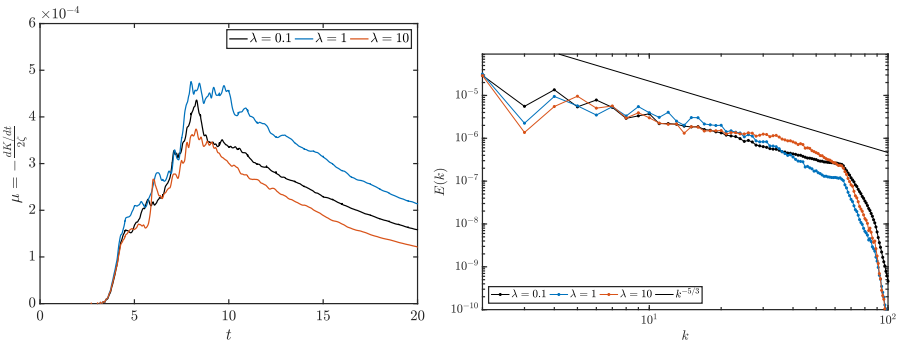

(a) Numerical viscosity (b) Kinetic energy spectra in $t = 14$

Fig. 6 Inviscid Taylor–Green vortex problem ($M_0 = 0.1$). The configuration is a periodic box with 32^3 elements and polynomial order $N = 3$. For the interfaces, we have used Roe Riemann solver with the lambda stabilisation $\lambda\text{diss}(u, \phi)$ as defined in (25). We have considered the values $\lambda = 0.1, 1$, and 10, whose results show clear parallelism with von Neumann analysis performed in Figure 5

was already noted in [10, 37, 25, 23]. We have also found that the amount of dissipation introduced is non–linearly controlled with λ, and that values above approximately $\lambda = 1$ yield lower dissipation rates. In this section, we study how this dissipation is introduced in the non–linear Euler equations. To do so, we solve the inviscid TGV problem (with Mach number $M_0 = 0.1$) introducing the λ stabilisation based on the Roe dissipation described in (24).

We construct a Cartesian with 32^3 elements and approximate the solution by order $N = 3$ polynomials. We represent the numerical dissipation for $t < 20$ in Figure 6(a). We have considered three λ values: 0.1 (low dissipation Roe), 1 (standard Roe), and 10 (hyper-upwind) [26]. Recall that the dissipation is only introduced numerically through the Riemann solver, since we consider the inviscid Euler equations (i.e. there is no physical viscosity). From the analysis of Fig. 6(a), we find that the maximum dissipation is achieved with $\lambda = 1$, which is in agreement with the von Neumann results in the previous section. Therefore, for $\lambda \lesssim 1$ increasing λ increases the scheme numerical dissipation,

but increasing λ for $\lambda \gtrsim 1$ yields the reverse effect, as demonstrated in von Neumann analysis (see Figure 5).

Figure 6(b) shows the kinetic energy spectra in $t = 14$. We find that all three λ values behave similarly in the low and medium wave–numbers range. At high wave–numbers, we find that the maximum dissipation is achieved by the standard Roe Riemann solver ($\lambda = 1$), whereas for the other two values there is some energy accumulation in the final part of the spectra. This energy accumulation is common when using central fluxes and it is also a side effect of the over–upwinding caused by the Lax–Friedrichs flux with low Mach numbers [33].

The simulation with $\lambda = 1$ can be regarded as an over–dissipated solution, i.e., the dissipation levels are higher than required and the energy spectra does not follow the theoretical $-5/3$ slope. This is enhanced with the use of lower numerical dissipation in the $\lambda = 0.1$ simulation. Note that $\lambda = 0.1$ is similar in spirit to the low dissipation Roe Riemann solver derived in [39] for $M_0 = 0.1$. Finally, Roe Riemann solver with $\lambda = 10$ suffers an accumulation of energy at high wave–numbers, as a result of its lack of dissipation compared to lower λ values (see Figure 6(a)).

3.3 Internal dissipation with the Spectral Vanishing Viscosity

In this section, we study the effect of the spectral vanishing viscosity method applied to discontinuous Galerkin schemes, using the framework introduced in Section 2.4.2. Only in this section, we use a constant SVV viscosity μ_{SVV} to emphasize the effect of the filtering operator introduced to the viscous fluxes.

3.3.1 Von Neumann analysis

This section studies the internal dissipation introduced by the SVV. We perform von Neumann analyses to the linear advection equation, (1) with the SVV flux described in (26), which uses the power kernel written in (27). Note that the SVV method obtains a standard second order derivative (a viscous flux) for $P_{SVV} = 0$, which is also introduced as a point of reference.

We depict von Neumann dissipation curves obtained with $\mu_{SVV} = 0.005$ ($\mathrm{Re}_{SVV} = aL/\mu_{SVV} = 200$) and we vary P_{SVV} in Figure 7(a), and its detailed view in Figure 7(b). This constant value of μ_{SVV} is only used in this section to provide an example of the behavior of the SVV. As expected, the SVV with $P_{SVV} = 0$ represents a second order derivative and behaves in the low wave–numbers range as $-k^2$, introducing low wave–number range dissipation. This is basically the impact of a standard Smagorinsky LES model in the discretization. The problem is that methods based on a second order derivative, which were developed in the Finite Volume community, tend to introduce non–vanishing dissipation even with smooth flows (e.g. laminar regimes), as reported in [46]. The SVV is specially useful to overcome this drawback, since it filters–out low frequency modes and prevents to dissipate smooth solutions.

In the default view of Figure 7(a), only a subtle difference is recognised since the effect of the SVV is concentrated in low and medium wave–numbers. Thus, to understand the effectiveness of the SVV, we check the dissipation curve zoomed at low and medium wave–numbers (Figure 7(b)). We show that the SVV, with the power kernel (27), is capable of controlling the shape of the dissipation curve between a pure viscous discretization ($P_{SVV} = 0$, labelled as NS) and the inviscid ($P_{SVV} >> 1$, labelled as Euler), thus enabling a precise control of the numerical dissipation introduced. The impact of the SVV in

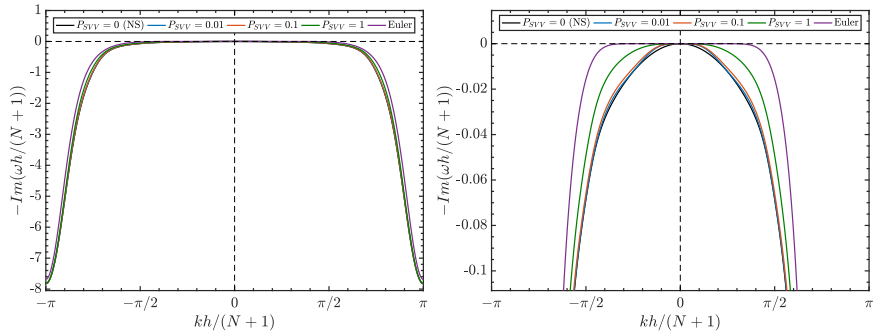

(a) Full view (b) Detailed view

Fig. 7 Von Neumann dissipation curves using SVV with upwind ($\lambda = 1$). Particularly, the effect of the SVV kernel power, P_{SVV}, is studied, where we have also included the particular cases with $P_{SVV} = 0$ (standard second order derivative), and the inviscid limit (Euler)

the dissipation may seem negligible since the overall difference between all curves is small. Nevertheless, we will show by means of numerical experiments that these small differences are capable to control the energy drain in under–resolved turbulent flow simulations.

3.3.2 Navier–Stokes problem

The linear von Neumann analysis shows that the SVV method allows us to modify and reshape the dissipation curve between that obtained with upwind Riemann solvers and that found for second order derivatives ($P_{SVV} = 0$). The SVV introduces dissipation mostly in low and medium wave–numbers. To test the SVV capabilities in the Euler equations, we consider the inviscid TGV problem (Appendix B). In this study we use a coarser Cartesian 4^3 mesh with $N = 8$ to test the SVV in a severely under–resolved configuration. In this section, we have adopted the low dissipation Roe L^2R [39] as Riemann solver (approximately equivalent to $\lambda \approx 0.1$ when $M_0 = 0.1$, although the scaling is performed with the local Mach number, cells with lower velocities will introduce less dissipation) as it was shown before (see Fig. 6(b)) that the

standard Roe ($\lambda = 1$) results in over-dissipated solutions for this problem. The SVV viscosity is set to $\mu_{SVV} = 0.005$ (equivalent to a Reynolds number $Re_{SVV} = 200$), and we study the effect of the kernel power coefficient by evaluating three values: $P_{SVV} = 0.1, 1$, and 10. We have chosen this value for the SVV viscosity since preliminary simulations showed an excess of dissipation for the selected mesh. The SVV approach removes the extra dissipation with filtering (controlled through P_{SVV}), instead of lowering the viscosity μ_{SVV}.

We depict the kinetic energy spectra at $t = 8$ in Figure 8, for the three SVV kernel power P_{SVV} values considered. We find that the energy decay at high wave–numbers is similar for all simulations, thus supporting von Neumann results (Figure 7(a)). At low and medium wave–numbers, we confirm the effectiveness of the SVV to shape the dissipation curve and adjust the energy spectra. We show that $P_{SVV} = 0.1$ yields a favourable result according to Figure 8, where the energy decays approximately following Kolmogorov's theoretical $k^{-5/3}$ rate [45], and is dissipated for high wave–numbers without producing energy accumulation. We find that both $P_{SVV} = 1$ and $P_{SVV} = 10$ present a lack of dissipation at medium wave–numbers, providing a LES configuration with unsatisfactory results, but that $P_{SVV} = 0.1$ provide satisfactory results.

Hence, the resulting scheme that combines upwind Riemann solvers and SVV is versatile, but requires an appropriate estimation of two parameters: the SVV viscosity μ_{SVV} and the kernel power P_{SVV}. Besides, a proper LES model (variable value of the turbulent viscosity) has not been included yet. We address these issues in the following section.

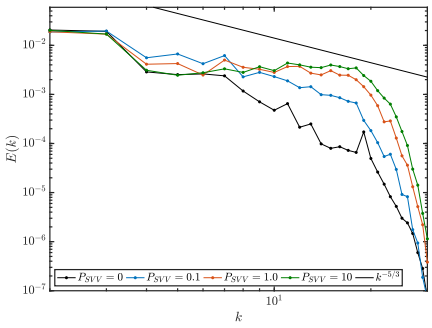

Fig. 8 Inviscid Taylor–Green vortex problem (with Mach number $M_0 = 0.1$) with 4^3 elements and polynomial order $N = 8$. We have used the SVV operator as defined in (28), where we set the SVV viscosity to $\mu_{SVV} = 0.005$ (equivalent to a $Re_{SVV} = 200$), and we vary the kernel power P_{SVV}. Note that the major difference between the standard Navier–Stokes discretization ($P_{SVV} = 0$) and the $P_{SVV} = 0.1$ scheme is dominant on low wave–numbers

4 Design of a Smagorisnky-SVV scheme

In Section 3.2 we have assessed the capabilities of upwind Riemann solvers to provide numerical dissipation at high wave–numbers, the capability of second order derivatives to introduce numerical dissipation at low and medium wave–numbers, and the potential of the SVV to shape the dissipation curve between pure elliptical discretizations ($P_{SVV} = 0$) and the inviscid equation. The latter has been found to effectively introduce dissipation at medium wave–numbers and (if required) also at low wave–numbers. In this section, we combine the strategies presented in the previous section to construct a scheme capable to provide accurate solutions in turbulent under–resolved flows. Hence, we study the effectiveness of a scheme combining a low dissipation Riemann solver to damp high wave–numbers and a SVV to dissipate medium wave–numbers to solve the inviscid TGV problem.

One of the drawbacks of the SVV is its requirement to estimate two parameters with a remarkable impact on the final solution, (see Figure 8). In an attempt to automatise the parameter selection, we set the SVV viscosity

in (29) to that specified by a standard Smagorinsky LES turbulence model as suggested in [18] and implemented in [34] in the context of continuous Galerkin methods,

$$\mu_{SVV} = \mu_t = C_S^2 \Delta^2 |\boldsymbol{S}|, \tag{33}$$

being $S_{ij} = \frac{1}{2}(\partial_j v_i + \partial_i v_j)$ the strain tensor, and such that only the P_{SVV} parameter remains free. One could argue that we have deleted one parameter (μ_{SVV}) to include a new one (C_S). However, we have found that the same value of $C_S = 0.2$ works in very different configurations, and the same applies to P_{SVV}. The developed Smaroginsky-SVV LES approach works for polynomial orders $N \geq 2$ and is specially well suited for higher orders, where the different scales can be clearly separated.

We consider the inviscid Taylor–Green vortex problem in a Cartesian mesh with 8^3 elements and two polynomial orders, $N = 4$ and $N = 8$, and we maintain the low dissipation Roe as Riemann solver. Both cases use the SVV method, with $\mu_{SVV} = \mu_t$. Figure 9 depicts the kinetic energy spectra varying the SVV kernel power P_{SVV}, and it also features the standard Smagorinsky LES model (without SVV) for comparison. We show that the resulting spectra, as in Figure 8 shows high dependence to the SVV power kernel, P_{SVV}. Precisely, for values $P_{SVV} > 0.1$ the dissipation provided by the method is not enough to control the accumulation of energy at high wave–numbers (recall that the higher the kernel power coefficient, the higher is the filtering performed to the viscosity introduced).

The standard Smagorinsky model presents an excessive dissipation when the flow is laminar, hence, decreasing the overall energy at further times [46]. This has been naturally avoided with the SVV technique, as it filters–out

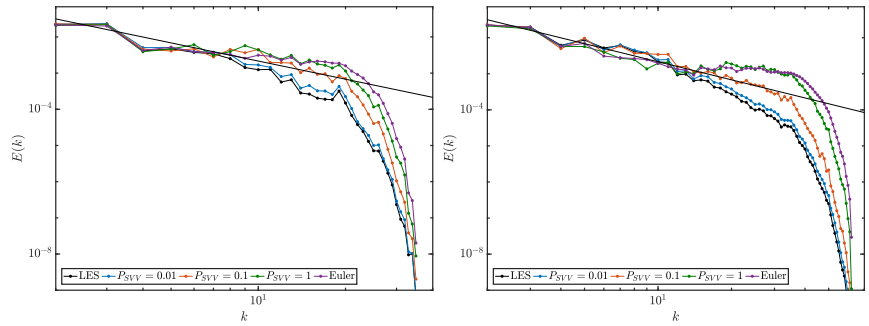

(a) Energy spectra with polynomial order $N = 4$

(b) Energy spectra with polynomial order $N = 8$

Fig. 9 Kinetic energy spectra in $t = 8$ obtained with the proposed Smagorinsky–SVV strategy for two polynomial orders. Both cases were computed using a 8^3 Cartesian mesh, solving the inviscid Taylor–Green vortex problem with Mach number $M_0 = 0.1$. Different values of the SVV kernel power P_{SVV} were studied

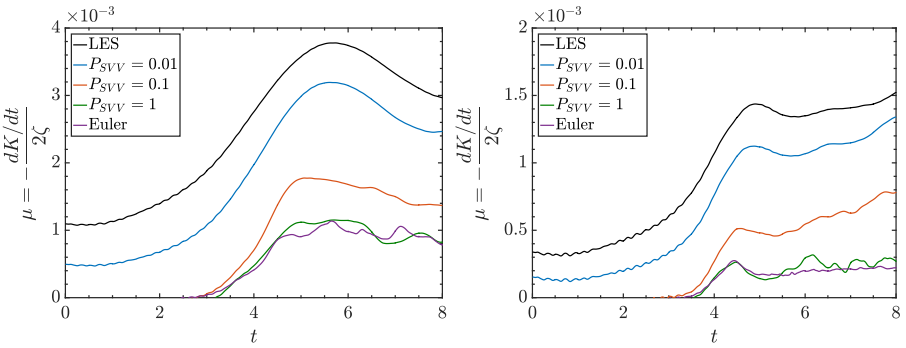

(a) Numerical viscosity with polynomial order $N = 4$

(b) Numerical viscosity with polynomial order $N = 8$

Fig. 10 Numerical viscosity introduced by the Smagorinsky–SVV strategy. Both cases were computed using a 8^3 Cartesian mesh. Different values of the SVV kernel power P_{SVV} were studied. Two effects are regarded: the capability of the SVV to remove the dissipation in the laminar region of the TGV problem ($t < 3$), and the lack of dissipation presented by the SVV with high kernel power coefficients

the laminar (smooth) energy components. For completeness, we represent the numerical viscosity introduced by both the Smagorinsky (LES) and the Smagorinsky–SVV LES in Figure 10. First, the laminar region (the region without subgrid–scales in the flow, $t < 3$) presents non–negligible numerical dissipation when using the standard Smagorinsky model, while this undesirable dissipation vanishes when considering the Smagorinsky–SVV approach.

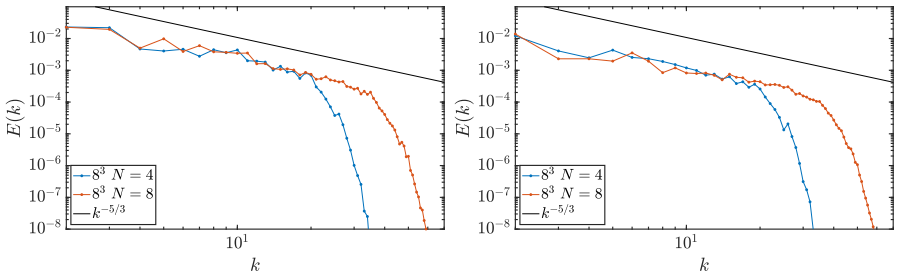

(a) $t = 8$ (b) $t = 14$

Fig. 11 Inviscid Taylor–Green vortex problem ($M_0 = 0.1$) kinetic energy spectra in $t = 8$ and $t = 14$ obtained with the Smagorinsky–SVV strategy using two different polynomial orders ($N = 4$ and $N = 8$). Both cases were computed using a 8^3 Cartesian mesh, and the SVV kernel power is $P_{SVV} = 0.1$

Second, we confirm the lack of dissipation presented by the SVV method with excessive kernel power P_{SVV}.

We conclude that the value $P_{SVV} = 0.1$ is appropriate for this test case. Lastly, we show the energy spectra for this configuration in Figure 11, showing that the turbulence model is not altered by the polynomial order. For completeness, we have also included the energy spectra for the decay phase $t = 14$ in Figure 11(b) to confirm that the method still follows the Kolmogorov's slope, and no energy accumulation is found in further times. In summary, the combination of the low dissipation Roe Riemann solver, the spectral vanishing viscosity, and the Smagorinsky model (which has been recently adopted in [20] as LES model in the context of DG solvers) as an input for μ_{SVV}, with the value $P_{SVV} = 0.1$ provides a robust method to simulate turbulent decay.

4.1 Assessment of the Smagorinsky–SVV scheme for a turbulent channel flow at $Re_\tau = 183$

We will test the developed Smagorinsky–SVV method in a wall–bounded turbulent channel. We maintain the parameters that provided accurate so-

lutions for the TGV problem: the SVV power kernel (27) with power coefficient $P_{SVV} = 0.1$, and the Smagorinksy model (33) with the standard value $C_S = 0.2$. The Smagorinsky model is complemented with Lilly's near wall treatment [47] to avoid non–zero (un–physical) turbulent viscosities near walls. For inviscid fluxes, we retain the $\mathrm{L}^2\mathrm{R}$ Riemann solver [39] and Pirozzoli's split form [31]. For time integration, we keep the third order Runge–Kutta scheme with $\mathrm{CFL} = 0.4$.

The only difference with the previous discretization rests in the discretization of the viscous terms. Due to the large velocity gradients experienced in this problem, the turbulent viscosity introduced by Smagorinsky's model is highly discontinuous at element interfaces. This leads to an oscillating LES solution if inter–element dissipation is not enough, which is the case if the Bassi–Rebay 1 scheme is used. Hence, we substitute the latter by the Symmetric Interior Penalty (SIP) method that penalizes inter–element discontinuities, and provides a smoother velocity field (and associated gradients), enabling a smooth LES flow.

The computational domain is a three–dimensional box, being the fluid confined between two planar walls (in the y–direction), and periodic boundaries in the remaining two directions. The stream–wise dimension is $L_x = 2\pi$, the wall normal direction dimension is $L_y = 2\delta$ (with the semi–wall distance $\delta = 1$), and lateral dimension $L_z = \pi$. We construct a mesh with equally spaced divisions $N_x = 8$, $N_y = 12$, and $N_z = 10$, where the solution is approximated with third order polynomials (which results in a coarse configuration leading to an under–resolved turbulent flow, as detailed later).

The Reynolds number is fixed to $\mathrm{Re}_\delta = U\delta/\nu = 3300$, based on the bulk velocity, or equivalently, $\mathrm{Re}_\tau = u_\tau\delta/\nu = 183$ based on the friction velocity u_τ, whose value is $u_\tau = 55.5 \cdot 10^{-3}$ m/s. The flow is driven by a constant

force estimated to achieve a time averaged velocity profile with mean velocity $U = 1$, $F_x = \rho u_\tau^2/\delta = 3.08 \cdot 10^{-3}$ N. The y^+ value for the first cell is $y^+ = 8.34$, which confirms that the simulation is clearly under–resolved. The initial condition is a Poiseuille profile, enriched with Gaussian noise to anticipate the transition onset. We run the simulation for 300 seconds, until the initial transients vanish. Then, we continue the simulation for 650 seconds, and compute averaged statistics in time and homogeneous spatial directions (only in the xz–directions) ,

$$\langle\phi\rangle(\mathbf{x}) = \frac{1}{N}\sum_{n=1}^{N}\phi(\mathbf{x}, t_n), \quad \langle\phi\rangle(y) = \int_{[0,2\pi]\times[0,\pi]} \langle\phi\rangle(x, y, z)\mathrm{d}x\mathrm{d}z, \tag{34}$$

where we get the averaged profiles $\langle\phi\rangle(y)$ as a function of the wall distance y. We average both velocities u_i and momentum $u_i u_j$ to get Reynolds stresses $\langle u_i' u_j'\rangle = \langle u_i u_j\rangle - \langle u_i\rangle\langle u_j\rangle$.

In Figure 12, we show the stream–wise mean velocity $u^+ = \langle u\rangle/u_\tau$ as a function of the wall distance $y^+ = y u_\tau/\nu$ (Figure 12(a)), and the off–diagonal component of the Reynolds stresses $-\langle u'v'\rangle/u_\tau^2$ as a function of the wall distance y/δ (Figure 12(b)). For the mean velocity, we consider the asymptotical law of the wall with $u^+ = y^+$ in the viscous sublayer ($y^+ < 5$) and $u^+ = \frac{1}{0.4}\ln y^+ + 5.5$ in the logarithmic region ($y^+ > 30$), both represented with dashed lines in Figure 12(a). For the Reynolds stresses, we compare with DNS solutions presented in [48], also represented with dashed line in Figure 12(b).

We consider three schemes, the Smagorinksy–SVV (abbreviated as SVV+LES), the standard Smagorinksy without SVV (LES), and the implicit LES (iLES) where all the dissipation rests on the Riemann solver and the physical viscosity. while the iLES is under–dissipated and the LES is over–dissipated,

the Smagorinsky–SVV LES scheme provides a solution comparable to the expected values (for both mean velocity and Reynolds stresses). These favouralbe results agree with the conclusions found for the TGV problem. Although in the near wall region the results differ from the DNS solution, we did not expect accurate results in this region given the very coarse mesh used near walls ($y^+ \simeq 8.34$) .

Overall, we find that the method presented in this work provides a remarkable improvement when compared to the standard Smagorinsky method in under–resolved configurations for wall bounded turbulent flows.

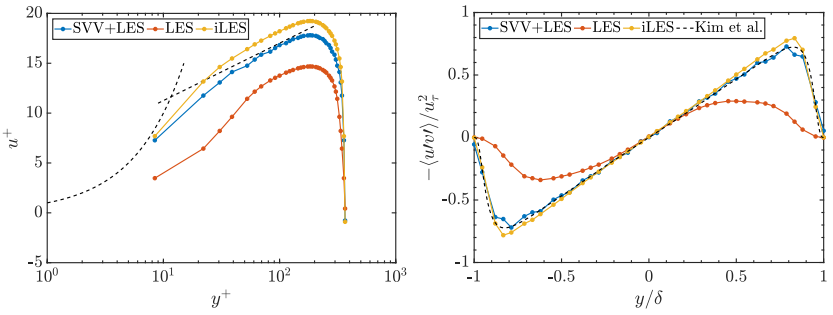

(a) Mean velocity profile $u^+ = \langle u \rangle / u_\tau$ (b) Reynolds stresses $-\langle u'v' \rangle / u_\tau^2$

Fig. 12 Channel flow statistics as a function of wall distance $y^+ = y u_\tau / \nu$. We consider three scheme: the Smagorinksy–SVV LES configuration (abbreviated as SVV+LES), the Smagorinsky LES model without SVV (LES), and the implicit LES (iLES). Dashed lines represent the law of the wall, in Figure 12(a), and DNS solutions from [48], in Figure 12(b).

5 Conclusions

We have presented a thorough study on the effect of different dissipation mechanisms for discontinuous Galerkin schemes that can be used to stabilise under–resolved simulations. We have first characterised their properties in wave–number space, by means of a linear von Neumann analysis (for a linear advection–diffusion equation), and then validated the model for transi-

tional/turbulent flows in the three–dimensional Taylor–Green Vortex Navier–Stokes problem.

We have studied the dissipation introduced by two different strategies: inter–element viscosity (upwind Riemann solvers) and internal viscosity (LES models and spectral vanishing viscosity). We have performed a linear analysis using von Neumann method to discover that the dissipation introduced by upwind Riemann solvers is not linear with parameter λ, which penalises the inter–element solution jumps. Instead, the dissipation introduced increases until a critical value is reached, to then decrease as the discretization tends to that of a conforming (i.e. continuous Galerkin) method. We have found that an upwind Riemann solver is required to maintain the dissipation introduced at high wave–numbers.

Next, we have studied the dissipation introduced by the Smagorinsky LES model and the spectral vanishing viscosity. On the one hand, we have found that the Smagorinsky LES model introduces an unnecessarily high level of dissipation. On the other hand, we have found that, the SVV with an appropriate filtering kernel, is capable of achieving high control on the dissipation introduced at low and medium wave–number regions, maintaining low dissipation when the flow is laminar.

Combining these ideas, we have proposed a Smagorinsky–SVV LES method, combined with a low dissipation Riemann solver. This Smagorinsky–SVV LES method is capable of maintaining low dissipation levels in laminar flows, while providing enough dissipation for increased Reynolds numbers. Our method has been calibrated with the Taylor–Green test case, and then challenged for an under–resolved channel flow at Reynolds number $Re_\tau = 183$, providing accurate statistics.

The presented Smagorinsky–SVV model has been designed based on classic von Neumann analysis. However, new methods based on spatial eigenvalue analyses [49, 50] may provide further insight into the developed turbulence model, and could complement the presented work.

Acknowledgments

This work was partially supported by the grant *Ayudas dirigidas al PDI para el fomento de la participación en solicitudes de proyectos H2020* from Universidad Politécnica de Madrid (Gonzalo Rubio). This work was partially supported by the grant *SIMOAIR (RTI2018-097075-B-I00)* from Ministerio Ciencia Innovacion y Universidades, and *SACOC (GA-831977)* from the European Commision (Eusebio Valero). The authors acknowledge the computer resources and technical assistance provided by the Centro de Supercomputación y Visualización de Madrid (CeSViMa).

A Compressible Navier–Stokes formulation

The 3D Navier–Stokes equations can be compactly written as,

$$\mathbf{u}_t + \nabla \cdot \boldsymbol{F}_e = \nabla \cdot \boldsymbol{F}_v, \tag{35}$$

where $\mathbf{u}$ is the vector of conservative variables $\mathbf{u} = [\rho, \rho v_1, \rho v_2, \rho v_3, \rho e]^T$, $\boldsymbol{F}_e$ are the inviscid, or Euler equations fluxes,

$$\boldsymbol{F}_e = \begin{bmatrix} \rho v_1 & \rho v_2 & \rho u_3 \\ \rho v_1^2 + p & \rho v_1 v_2 & \rho v_1 v_3 \\ \rho v_1 v_2 & \rho v_2^2 + p & \rho v_2 v_3 \\ \rho v_1 v_3 & \rho v_2 v_3 & \rho v_3^2 + p \\ \rho v_1 H & \rho v_2 H & \rho v_3 H \end{bmatrix}, \tag{36}$$

where ρ, e, H and p are the density, total energy, total enthalpy, and pressure respectively, and $\mathbf{v} = [v_1, v_2, v_3]^T$ is the velocity. Additionally, $\mathbf{F}_v$ defines the viscous fluxes,

$$\mathbf{F}_v(\mu, \mathbf{v}, \nabla\mathbf{v}) = \begin{bmatrix} 0 & 0 & 0 \\ \tau_{xx} & \tau_{xy} & \tau_{xz} \\ \tau_{yx} & \tau_{yy} & \tau_{yz} \\ \tau_{zx} & \tau_{zy} & \tau_{zz} \\ \sum_{j=1}^{3} v_j\tau_{1j} + \kappa T_x & \sum_{j=1}^{3} v_j\tau_{2j} + \kappa T_y & \sum_{j=1}^{3} v_j\tau_{3j} + \kappa T_z \end{bmatrix}, \tag{37}$$

where κ is the thermal conductivity, T_x, T_y and T_z denote the gradients of temperature and the stress tensor $\boldsymbol{\tau}$ is defined as $\boldsymbol{\tau} = \mu(\nabla\mathbf{v} + (\nabla\mathbf{v})^T) - 2/3\mu\boldsymbol{I}\nabla\cdot\mathbf{v}$, with μ the dynamic viscosity, and $\boldsymbol{I}$ is the three-dimensional identity matrix.

We discretise Euler equations using the novel nodal DG split–formulation derived in [31] (precisely, we use Pirozzoli split formulation), while for viscous fluxes we use the Bassi-Rebay 1 (BR1) scheme [51]. Implementation details regarding the split–form scheme can be found in Appendix A. In all cases, the Mach number is kept to 0.1 such that compressible effects are negligible. We highlight how split–forms are implemented in one dimension recovering the inviscid version of the weak form (21),

$$\int_{el} \mathbf{u}_t \cdot \phi_j + (\boldsymbol{F}^{\star}{}_e - \boldsymbol{F}_e)\,\phi_j \Big|_{-1}^{1} - \int_{el} (\mathbf{F}_e)_x\,\phi_j = 0 \tag{38}$$

Usually, in the standard DG method, the fluxes divergence $(F_e)_x$ is obtained by direct differentiation of the Lagrange polynomials,

$$(\mathbf{F}_e)_x(\xi_i) = \sum_{j=0}^{N} \mathbf{F}_e(u_j) l_j'(\xi_i) = \sum_{j=0}^{N} \mathbf{F}_e(u_j) D_{ij}. \tag{39}$$

However, in the split–form approach, this divergence is approximated by a two–point kinetic energy conserving (Pirozzoli) numerical volume flux $\mathbf{F}_e^{\sharp}(\mathbf{u}_i, \mathbf{u}_m)$,

$$\mathbf{F}_e^\sharp(\mathbf{u}_i,\mathbf{u}_m) = \begin{pmatrix} \{\!\{\rho\}\!\}\,\{\!\{v_1\}\!\} \\ \{\!\{\rho\}\!\}\,\{\!\{v_1\}\!\}^2 + \{\!\{p\}\!\} \\ \{\!\{\rho\}\!\}\,\{\!\{v_1\}\!\}\,\{\!\{v_2\}\!\} \\ \{\!\{\rho\}\!\}\,\{\!\{v_1\}\!\}\,\{\!\{v_3\}\!\} \\ \{\!\{\rho\}\!\}\,\{\!\{v_1\}\!\}\,\{\!\{H\}\!\} \end{pmatrix} \tag{40}$$

which allows to write,

$$\left(\mathbf{F}_e\right)_x(\xi_i) \approx \sum_{m=0}^{N} 2D_{im}\mathbf{F}_e^\sharp(\mathbf{u}_i,\mathbf{u}_m). \tag{41}$$

The extension to three dimensions with curvilinear elements can be found in [31, 32].

B Taylor–Green vortex problem

Numerical experiments are performed to evaluate the validity of von Neumann analysis assessments in the more general case of the NSE. To test the under–resolved capabilities of the strategies studied with von Neumann analysis, we will solve the Taylor–Green Vortex (TGV) problem [52]. The TGV problem has been widely used to report the subgrid–scale modelling capabilities of iLES approaches and discretizations [31, 53]. In this paper, we assess von Neumann analysis truthfulness to estimate the dissipation introduced by the operators introduced in Sections 2.4.1 and 2.4.2. The configuration of the TGV problem is a three dimensional periodic box $[-\pi,\pi]^3$ with the initial condition,

$$\begin{aligned} \rho &= \rho_0, \\ v_1 &= V_0 \sin x \cos y \cos z, \\ v_2 &= -V_0 \cos x \sin y \cos z, \\ v_3 &= 0, \\ p &= \frac{\rho_0 V_0^2}{\gamma M_0^2} + \frac{\rho_0 V_0^2}{16}(\cos 2x + \cos 2y)(\cos 2z + 2). \end{aligned} \tag{42}$$

The Mach number is $M_0 = 0.1$ in all the simulations performed herein. The reported quantities to measure the simulations accuracy are the kinetic energy rate,

$$\epsilon = -\frac{dK}{dt} = -\frac{1}{|\Omega|}\frac{d}{dt}\int_{\Omega}\frac{1}{2}\rho V^2 d\boldsymbol{x}, \tag{43}$$

the enstrophy,

$$\zeta = \frac{1}{2|\Omega|}\int_{\Omega}(\nabla\times\boldsymbol{v})^2 d\boldsymbol{x}, \tag{44}$$

the numerically introduced dissipation estimated with both ϵ and ζ [12],

$$\mu \simeq \frac{\epsilon}{2\zeta} = -\frac{dK/dt}{2\zeta}, \tag{45}$$

and the kinetic energy spectra, measured at a fixed time snapshot ($t = 8$ to observe transitional flow, and $t = 14$ to show the isotropic decay). In this paper we consider both the inviscid version of the Taylor–Green vortex problem, and the viscous Taylor–Green vortex problem with Reynolds number $Re = 1600$. Finally, all Navier–Stokes simulations are time-marched using a three stage Runge–Kutta scheme with a Courant–Friedrichs–Lewy (CFL) number of 0.4.

References

1. F. Bassi and S. Rebay, A high-order accurate discontinuous finite element method for the numerical solution of the compressible Navier-Stokes equations, Journal of Computational Physics 131 (2) (1997) 267 – 279.
2. E. Ferrer, An interior penalty stabilised incompressible Discontinuous Galerkin - Fourier solver for implicit Large Eddy Simulations, Journal of Computational Physics 348 (2017) 754–775.
3. M. Kompenhans, G. Rubio, E. Ferrer, and E. Valero, Adaptation strategies for high order discontinuous Galerkin methods based on tau-estimation, Journal of Computational Physics 306 (2016) 216 – 236.
4. M. Kompenhans, G. Rubio, E. Ferrer, and E. Valero, Comparisons of p–adaptation strategies based on truncation– and discretisation–errors for high order discontinuous Galerkin methods, Computers & Fluids 139 (2016) 36 – 46, 13th {USNCCM} International Symposium of High-Order Methods for Computational Fluid Dynamics - A special issue dedicated to the 60th birthday of Professor David Kopriva.

5. E. Ferrer and R.H.J. Willden, A high order discontinuous Galerkin finite element solver for the incompressible Navier–Stokes equations, Computers & Fluids 46 (1) (2011) 224–230.
6. E. Ferrer and R. H.J. Willden, A high order discontinuous Galerkin - Fourier incompressible 3D Navier-Stokes solver with rotating sliding meshes, Journal of Computational Physics 231 (21) (2012) 7037–7056.
7. E. Ferrer, D. Moxey, R.H.J. Willden and S. Sherwin, Stability of projection methods for incompressible flows using high order pressure-velocity pairs of same degree: continuous and discontinuous Galerkin formulations, Communications in Computational Physics 16 (3) (2014) 817–840.
8. F. Fraysse, C. Redondo, G. Rubio, and E. Valero, Upwind methods for the Baer–Nunziato equations and higher-order reconstruction using artificial viscosity, Journal of Computational Physics 326 (2016) 805 – 827.
9. J. Manzanero, G. Rubio, D. A. Kopriva, E. Ferrer, E. Valero, Entropy-stable discontinuous Galerkin approximation with summation-by-parts property for the incompressible Navier-Stokes/Cahn-Hilliard system, arXiv preprint arXiv:1910.11252.
10. J.S. Hesthaven and T. Warburton, Nodal discontinuous Galerkin methods: algorithms, analysis, and applications, Springer Science & Business Media, 2008.
11. R.M. Kirby and G.E. Karniadakis, De-aliasing on non-uniform grids: Algorithms and applications, Journal of Computational Physics 191 (1) (2003) 249–264.
12. G.J. Gassner and A.D. Beck, On the accuracy of high-order discretizations for under-resolved turbulence simulations, A.D. Theoretical and Computational Fluid Dynamics. (2013) 27–221.
13. R.C. Moura, G. Mengaldo, J. Peiró and S.J. Sherwin, On the eddy-resolving capability of high-order discontinuous Galerkin approaches to implicit LES / under-resolved DNS of Euler turbulence, Journal of Computational Physics 330 (2017) 615 – 623.
14. E. Lenormand, P. Sagaut, L.T. Phuoc and P. Comte, Subgrid-Scale Models for Large-Eddy Simulations of Compressible Wall Bounded Flows, AIAA Journal 38 (8) (2000) 1340–1350.
15. T.J.R. Hughes, A.A. Oberai and L. Mazzei, Large eddy simulation of turbulent channel flows by the variational multiscale method, Physics of Fluids 13 (6) (2001) 1784–1799.
16. R.M. Kirby and S.J. Sherwin, Stabilisation of spectral/hp element methods through spectral vanishing viscosity: application to fluid mechanics modelling, Computer Methods in Applied Mechanics and Engineering 195 (23-24) (2006) 3128–3144.

17. E. Tadmor, Convergence of spectral methods for nonlinear conservation laws, SIAM Journal on Numerical Analysis 26 (1) (1989) 30–44.
18. G.S. Karamanos and G.E. Karniadakis, A spectral vanishing viscosity method for large-eddy simulations, Journal of Computational Physics 163 (1) (2000) 22 – 50.
19. C.C. de Wiart, K. Hillewaert, M. Duponcheel and G. Winckelmans, Assessment of a discontinuous Galerkin method for the simulation of vortical flows at high Reynolds number, International Journal for Numerical Methods in Fluids 74 (7) 469–493.
20. David Flad and Gregor Gassner, On the use of kinetic energy preserving DG-schemes for large eddy simulation, Journal of Computational Physics 350 (Supplement C) (2017) 782 – 795.
21. N. Fehn, W.A. Wall and M. Kronbichler, On the stability of projection methods for the incompressible Navier–Stokes equations based on high-order discontinuous Galerkin discretizations, Journal of Computational Physics 351 (2017) 392 – 421.
22. M. de la Llave Plata, V. Couaillier and M.C. le Pape, On the use of a high-order discontinuous Galerkin method for DNS and LES of wall-bounded turbulence, Computers and Fluids.
23. M. Alhawwary, Z. Wang, Fourier analysis and evaluation of DG, FD and compact difference methods for conservation laws, Journal of Computational Physics 373 (2018) 835 – 862.
24. R. C. Moura, P. Fernandez, G. Mengaldo, S. J. Sherwin, Temporal eigenanalysis of HDG methods for linear advection–diffusion.
25. G.J. Gassner and D.A. Kopriva, A comparison of the dispersion and dissipation errors of Gauss and Gauss-Lobatto discontinuous Galerkin spectral element methods, SIAM Journal on Scientific Computing 33 (5) (2011) 2560–2579.
26. R.C. Moura, S.J. Sherwin, and J. Peiro, Linear dispersion-diffusion analysis and its application to under-resolved turbulence simulations using discontinuous Galerkin spectral/hp methods, Journal of Computational Physics 298 (2015) 695–710.
27. J. Manzanero, G. Rubio, E. Ferrer and E. Valero, Dispersion-dissipation analysis for advection problems with nonconstant coefficients: Applications to discontinuous Galerkin formulations, SIAM Journal on Scientific Computing 40 (2) (2018) A747–A768.
28. P. Fernandez, R. C. Moura, G. Mengaldo, J. Peraire, Non-modal analysis of spectral element methods: Towards accurate and robust large-eddy simulations, Computer Methods in Applied Mechanics and Engineering 346 (2019) 43 – 62.
29. D.A. Kopriva and G.J. Gassner, An energy stable discontinuous Galerkin spectral element discretization for variable coefficient advection problems, SIAM Journal on Scien-

tific Computing 36 (4) (2014) A2076–A2099.

30. J. Manzanero, G. Rubio, E. Ferrer, E. Valero and D.A. Kopriva, Insights on aliasing driven instabilities for advection equations with application to Gauss-Lobatto discontinuous Galerkin methods, Journal of Scientific Computing.
31. G.J. Gassner, A.R. Winters and D.A. Kopriva, Split form nodal discontinuous Galerkin schemes with Summation-By-Parts property for the compressible Euler equations, Journal of Computational Physics, in Press.
32. G.J. Gassner, A. Winters, Andrew, F. Hindenlang, D.A. Kopriva, The BR1 scheme is stable for the compressible Navier–Stokes equations.
33. A. R. Winters, R. C. Moura, G. Mengaldo, G. J. Gassner, S. Walch, J. Peiro, S. J. Sherwin, A comparative study on polynomial dealiasing and split form discontinuous galerkin schemes for under-resolved turbulence computations, Journal of Computational Physics 372 (2018) 1 – 21.
34. R.M. Kirby and G.E. Karniadakis, Coarse Resolution Turbulence Simulations With Spectral Vanishing Viscosity–Large-Eddy Simulations (SVV-LES), Journal of Fluids Engineering 124 (4) (2002) 886–891.
35. D.A. Kopriva, Implementing spectral methods for partial differential equations, Springer Netherlands, 2009.
36. D.N. Arnold, F. Brezzi, B. Cockburn, and L.D. Marini, Unified analysis of discontinuous Galerkin methods for elliptic problems, SIAM J. Numer. Anal. 39 (5) (2001) 1749–1779.
37. R.C. Moura, S.J. Sherwin, and J. Peiró, Eigensolution analysis of spectral/hp continuous Galerkin approximations to advection–diffusion problems: Insights into spectral vanishing viscosity, Journal of Computational Physics 307 (2016) 401–422.
38. J. Manzanero, A.M. Rueda–Ramírez, G. Rubio and E. Ferrer, The Bassi Rebay 1 scheme is a special case of the Symmetric Interior Penalty formulation for discontinuous Galerkin discretisations with Gauss–Lobatto points, Journal of Computational Physics 363 (2018) 1 – 10.
39. K. Oßwald, A. Siegmund, P. Birken, V. Hannemann and A. Meister, L^2Roe: a low dissipation version of Roe's approximate Riemann solver for low Mach numbers, International Journal for Numerical Methods in Fluids 81 (2) (2016) 71–86.
40. T.C. Fisher and M.H. Carpenter, High-order entropy stable finite difference schemes for nonlinear conservation laws: Finite domains, Journal of Computational Physics 252 (2013) 518–557.
41. G.J. Gassner, A skew-symmetric discontinuous Galerkin spectral element discretization and its relation to SBP-SAT finite difference methods, SIAM Journal on Scientific

Computing 35 (3) (2013) 1233–1256.

42. E. Toro, Riemann solvers and numerical methods for fluid dynamics, Springer, 2009.
43. B. Guo, and H. Ma and E. Tadmor, Spectral vanishing viscosity method for nonlinear conservation laws, SIAM Journal on Numerical Analysis 39 (4) (2001) 1254–1268.
44. J. Smagorinsky, General circulation experiments with the primitive equations, Monthly Weather Review 91 (3) (1963) 99–164.
45. S.B. Pope, Turbulent Flows, Cambridge University Press, 2000.
46. P. Fernández, N.C. Nguyen, and J. Peraire, Subgrid-scale modeling and implicit numerical dissipation in DG-based large-eddy simulation, in: 23rd AIAA Computational Fluid Dynamics Conference, 2017.
47. D. K. Lilly, A proposed modification of the germano subgrid-scale closure method, Physics of Fluids A: Fluid Dynamics 4 (3) (1992) 633–635.
48. J. Kim, P. Moin, R. Moser, Turbulence statistics in fully developed channel flow at low reynolds number, Journal of Fluid Mechanics 177 (1987) 133–166.
49. G. Mengaldo, D. D. Grazia, R. Moura, S. Sherwin, Spatial eigensolution analysis of energy-stable flux reconstruction schemes and influence of the numerical flux on accuracy and robustness, Journal of Computational Physics 358 (2018) 1–20.
50. G. Mengaldo, R. Moura, B. Giralda, J. Peiró, S. Sherwin, Spatial eigensolution analysis of discontinuous Galerkin schemes with practical insights for under-resolved computations and implicit LES, Computers & Fluids 169 (2018) 349–364.
51. F. Bassy and S. Rebay, High-order accurate discontinuous finite element solution of the 2D Euler equations, Journal of Computational Physics 138 (1997) 251–285.
52. G.I. Taylor and A.E. Green, Mechanism of the production of small eddies from large ones, in: Proceedings of The Royal Society A: Mathematical, Physical and Engineering Sciences, Vol. 158, 1937, pp. 499–521.
53. R.C. Moura, G. Mengaldo, J. Peiró and S.J. Sherwin, An LES Setting for DG-Based Implicit LES with Insights on Dissipation and Robustness, Springer International Publishing, Cham, 2017, pp. 161–173.